Building Intermixed Donor-Acceptor Architectures for Water-Processable Organic Photovoltaics

Melissa Marks[a], Natalie P. Holmes[a*], Anirudh Sharma[b,c], Xun Pan[b], Riku Chowdhury[a], Matthew G. Barr[a], Coralie Fenn[a], Matthew J. Griffith[a], Krishna Feron[a], A.L. David Kilcoyne[d], David A. Lewis[b], Mats R. Andersson[b], Warwick J. Belcher[a], Paul C. Dastoor[a]

[a] Centre for Organic Electronics, University of Newcastle, University Drive, Callaghan NSW 2308, Australia

[b] Flinders Institute for Nanoscale Science and Technology, Flinders University, Sturt Road, Bedford Park, Adelaide, SA 5042, Australia

[c] Laboratoire de Chimie des Polymères Organiques (LCPO), University of Bordeaux, UMR 5629, B8 Allée Geoffroy Saint Hilaire, 33615 Pessac Cedex, France

[d] Advanced Light Source, Lawrence Berkeley National Laboratory, Berkeley, CA 94720, USA

*Corresponding author: Natalie P. Holmes, Natalie.Holmes@newcastle.edu.au

ABSTRACT

A modified synthesis method for aqueous nanoparticle printing inks, based upon vacuum-assisted solvent removal, is reported. Poly(3-hexylthiophene) : phenyl C_{61} butyric acid methyl ester nanoparticle inks were prepared via this modified miniemulsion method; leading to both an improvement in photoactive layer morphology and a substantial reduction in the ink fabrication time. A combination of UV-visible spectroscopy, photoluminescence spectroscopy and scanning transmission X-ray microscopy measurements revealed a nanoparticle morphology comprised of highly intermixed donor-acceptor domains. Consistent with these measurements, dynamic mechanical thermal analysis of the nanoparticles showed a glass transition temperature (T_g) of 104 °C, rather than a pure polymer phase or pure fullerene phase T_g. Together the spectroscopy, microscopy and thermomechanical data indicate that rapid solvent removal generates a more blended nanoparticle morphology. As such, this study highlights a new experimental lever for optimising nanostructure in the photoactive layer of nanoparticulate organic photovoltaic devices by enabling highly intermixed donor-acceptor architectures to be built from customised nanoparticulate inks.

1. Introduction

As the global demand for energy increases, the need for renewable sources becomes more pressing.[1] Organic photovoltaics (OPVs) are an attractive option which have received increasing attention in recent years, due to their potential as low-cost, light-weight, semi-transparent and flexible devices, allowing for their use in applications for which conventional silicon-based PVs are unsuitable.[2–5] Record efficiencies of OPV devices have now increased beyond 14%,[6] and lifetimes greater than 5 years have been measured under operating conditions.[7]

One specific draw-back of many of the current higher-performing OPV designs is that photoactive layers are generally deposited from toxic organic solvents.[8] Hence, a major challenge of upscaling the production of OPV technology is choosing processing solvents that meet health and safety standards without increasing manufacturing cost.[9–11] Fortunately, emerging colloidal nanoparticle ink technology has enabled photoactive layers to be processed using environmentally-friendly solvents, such as water and ethanol,[12–15] which are relatively cheap and have no associated health or safety concerns. Additionally, these nanoparticle photoactive layers allow for a level of morphological control, prior to film deposition, which is not available for other active layers.[16] The size of the nanoparticles in these films can be controlled with slight variations in the production process, such that the donor-acceptor material domain sizes are closer to optimal.[17]

Two key methods of producing nanoparticle dispersions for OPV applications are the miniemulsion method[18] and the precipitation method.[19,20] Early devices using nanoparticle active layer films produced via the miniemulsion process had a maximum power conversion efficiency (PCE) of 0.55%.[12] In subsequent years, efficiencies have increased considerably, up to 3.8% using the miniemulsion method by combining PBDTTPD and $PC_{71}BM$.[21] When employing the precipitation method, efficiencies of up to 4.5% have been achieved using P3HT and ICBA.[22] Further improving the morphology of these active layers has been identified as a key avenue for increasing NP OPV device performance,[23] and research in this area is ongoing. Device performance is affected by the internal morphology of the nanoparticles themselves, as well as the resulting films, and methods exist for altering both.[24–26] As an example, the internal morphology of the nanoparticles can be controlled by changing the donor-acceptor ratio used in the production of the nanoparticle dispersion.[17,27] Film morphology can be modified by post-deposition thermal treatments; heating the films above the glass transition temperature (T_g) of

the materials (or of the blend itself) leads to changes in the blend film morphology that can improve charge transport.[28]

Studies focusing on the optimisation of bulk heterojunction (BHJ) morphologies have demonstrated that highly intermixed donor and acceptor domains allow for improved exciton dissociation, and nanoscale phase separation is necessary for charge transportation, resulting in higher OPV device performance.[29–31] Herein we investigate a modified miniemulsion nanoparticle fabrication method to generate a particle morphology with more intermixed donor-acceptor material phases in an effort to more closely match the optimal BHJ morphology of solvent-cast OPV devices, but without the negative consequences of chlorinated solvent use. The poly(3-hexylthiophene) : phenyl C_{61} butyric acid methyl ester (P3HT:PC$_{61}$BM) material system was chosen as it represents a well-characterised system in the field of NP OPV and hence the existing literature forms an excellent platform for comparison when investigating this modified miniemulsion fabrication method. We have utilised a combination of microscopy, spectroscopy and thermomechanical methods to investigate the nanoparticle morphology, and the impact of this altered nanoparticle morphology was further investigated by considering the device performance and exciton dissociation efficiency (η_{ED}) of NP OPVs fabricated using this modified procedure.

2. Methods

2.1 Materials

P3HT was synthesised as described by Holmes *et al.*,[24] with an M_n of 16,770 g mol^{-1}, M_w of 22,270 g mol^{-1} and PDI of 1.33 as measured by gel permeation chromatography (GPC), with further details reported elsewhere.[26] PC$_{61}$BM was synthesised at the Centre for Organic Electronics, University of Newcastle, Australia, following the procedure of Hummelen *et al.*[32] Chloroform and sodium dodecyl sulphate (SDS) were purchased from Sigma Aldrich. Poly(3,4-ethylenedioxythiophene):poly(styrene) sulfonate (PEDOT:PSS) Clevios HTL Solar was purchased from Heraeus and filtered through a 0.45 μm PVDF filter prior to use. Pre-patterned indium tin oxide (ITO) substrates were purchased from Xinyan Technology Ltd.

2.2 Nanoparticle Fabrication

15 mg of P3HT and 15 mg of PC$_{61}$BM (1:1 donor-acceptor ratio) were dissolved in 560 μl of chloroform and 33 mg of SDS surfactant was dissolved in 2.78 ml of MilliQ purified water. The aqueous and organic phases were combined to produce a macroemulsion before sonication

to generate a minemulsion (Figure 1A) on a Hielscher UP400S at 50 % amplitude for 2 minutes with a surrounding ice bath in place. The miniemulsion was then transferred to a 50 ml round bottom flask and chloroform was removed using a rotary evaporator over 3 minutes (Figure 1B), however a colour change from orange (miniemulsion) to purple (nanoparticle dispersion) along with the absence of bubbling in the liquid after 12 seconds of rotary evaporation indicated that all chloroform was removed from the miniemulsion within the first 12 seconds. Maximum rotation speeds (180 RPM), a water bath temperature of 60 °C and pressure setting of 400 Torr were used. The system was vented periodically during the evaporation to prevent foaming (due to the presence of surfactant) and loss of material.
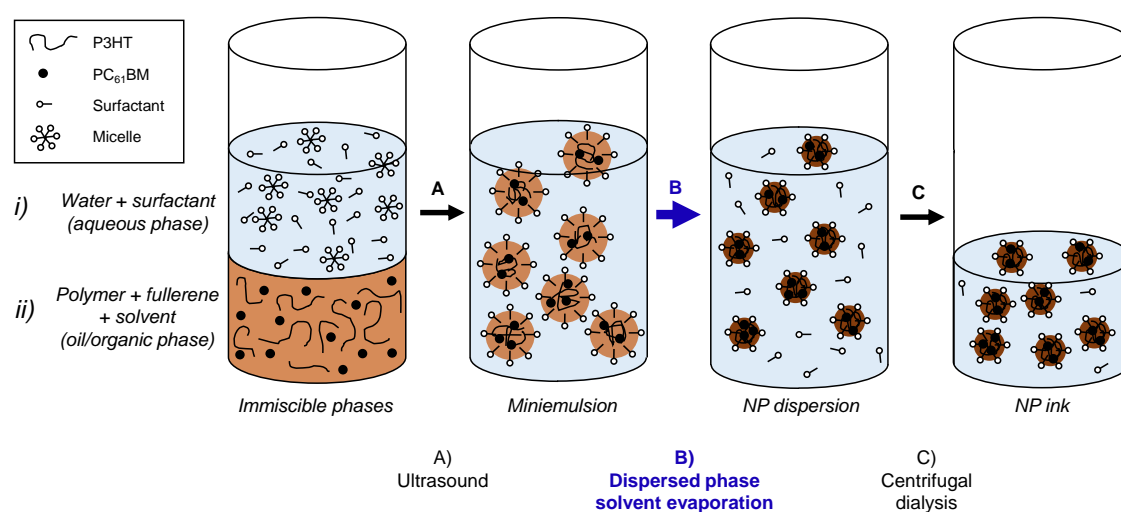

Figure 1. Schematic depicting the miniemulsion process for the fabrication of organic nanoparticles of P3HT:$PC_{61}BM$ with the dispersed phase solvent evaporation step (B) highlighted in blue. Step B has been accelerated in the study by employing a vacuum-assisted dispersed oil phase solvent removal.

The standard miniemulsion procedure was used to fabricate nanoparticle inks with a slow chloroform evaporation step (method reported elsewhere),[28] the only difference being the chloroform evaporation, which was performed overnight on a hotplate at 60 °C over a period of 16 hours, with stirring at 1200 RPM.

The nanoparticle ink was then transferred by pipette to a dialysis tube, and the inks were dialysed by centrifugal dialysis to remove excess free surfactant and to concentrate the inks using a Hettich Zentrifugen Rotina 420 (Figure 1C), consistent with our previously reported method.[28] This dialysis process achieved an ink solids loading of 6 wt%.

2.3 Spectroscopy

Nanoparticle films were spin coated on quartz glass substrates for PL measurements and stored under nitrogen, with spin conditions chosen to match OPV fabrication conditions (1750 RPM). Samples were removed one at a time from the nitrogen glovebox, and photoluminescence (PL) measurements were performed under a nitrogen environment. After taking initial PL measurements of unannealed nanoparticle films, the films were annealed under nitrogen and re-measured. The annealing conditions were chosen to match the OPV annealing conditions (as cast, dried at 110 °C for 4 min, and dried then annealed for 4 min at 80 °C). PL measurements were made on a Shimadzu RF-6000 spectrofluorophotometer with a beam to sample angle of 65 degrees, $\lambda_{exc} = 500$ nm, $\lambda_{em} = 400 - 900$ nm, excitation bandwidth = 5 nm, emission bandwidth = 10 nm. A 420 nm high-pass cut-off filter was placed in the path of the beam before the sample. For PL measurements of nanoparticle inks in the liquid state, measurements were made in a quartz cuvette and all instrument settings were the same except for the excitation and emission bandwidth which were both set to 20 nm. Nanoparticle inks were diluted 1/1000 with water for liquid state (cuvette) PL and UV–Vis measurements. UV–Vis measurements were taken using an ultraviolet–visible absorption spectrophotometer (UV–Vis, Varian Cary 6000i) in the wavelength range 300–900 nm. Spin coating conditions and annealing conditions of nanoparticle films prepared for all UV–Vis measurements were matched to conditions used for OPV and PL measurements.

2.4 Microscopy

Samples were prepared for scanning transmission X-ray microscopy (STXM) by spin coating 2.5 μl nanoparticle dispersion onto low stress silicon nitride (Si_3N_4) windows with silicon dioxide coating (window dimensions 0.25 x 0.25 mm^2, window thickness 15 nm, frame 5 x 5 mm^2) at 3000 RPM, 1 min., acceleration of 112 RPM/s. Nanoparticles prepared for STXM morphological investigation had a reduced concentration of surfactant in the miniemulsion aqueous phase (0.36 mg/ml) with the aim of achieving both larger particles and a broad distribution in particle size for imaging. These large nanoparticles had a diameter >100 nm. Unannealed (or 'as cast') samples were air dried. STXM measurements were performed at the Advanced Light Source on beamline 5.3.2.2,[33] with the full method reported elsewhere.[28]

After STXM measurements, the samples with deposited nanoparticles were transported back to the University of Newcastle (Australia), and transmission electron microscopy (TEM) was used to re-image the same regions of the sample where possible. A JEOL 1200 EXII was used at an accelerating voltage of 80 kV and at varying magnification ranges.

Samples were prepared for scanning electron microscopy (SEM) by spin coating 2.5 μl of nanoparticle ink onto a conductive silicon substrate (3000 RPM, 1 min, low acceleration of 112 RPM/s). A Zeiss Sigma VP field emission SEM (FESEM) was used at an accelerating voltage of 2 kV, and magnification ranges of 10,000–300,000x.

Focused ion beam milling and scanning electron microscopy (FIB-SEM) was performed on a FEI Helios NanoLab 600 Dual Beam instrument equipped with the energy dispersive X-ray spectroscopy (EDS) detector from EDAX. NP OPV samples were first coated with a 3-5 nm Au layer using an EMITECH K550X sputter coater in order to form a conductive layer on the sample surface to dissipate electron-induced charging. Once samples were loaded into the FIB-SEM instrument, to form a sacrificial top surface for FIB milling a 20 μm × 1 μm Pt patch (thickness 15-20 nm) was deposited using a gas injection system, with $(CH_3)_3Pt(CpCH_3)$ gas. FIB trenches were milled with a Ga ion beam to form cross-sectional views of the layered structure of ITO/PEDOT:PSS/P3HT:PC_{61}BM RE-NP/ZnO/Al OPV devices. SEM images were collected of the cross-sectional face at an angle of 52° and an accelerating voltage of 5 kV, and measurements of layer thickness were corrected for angle by the FEI xT software.

Atomic force microscopy (AFM) images were collected using an Asylum Research Cypher in AC mode. Soft tapping mode Tap150Al-G AFM tips were supplied by Budget Sensors (resonant frequency: 150 kHz, force constant: 5 N/m). Nanoparticle films were coated onto glass/ITO/PEDOT:PSS substrates to replicate the underlying surface in the OPV device structure.

2.5 Thermomechanical analysis

Dynamic mechanical thermal analysis (DMTA) was performed on a TA Q800 DMA in strain-controlled mode with a frequency of 1 Hz, amplitude of 5 μm, temperature ramp of 3 °C/min, temperature range of -110 to 300 °C and under a nitrogen environment (60 mL/min). The first scan was run from room temperature to 30 °C to remove possible moisture from the samples. Samples were prepared for DMTA by drop-casting nanoparticle inks onto woven glass fibre mesh substrates cut at a 45° angle towards the direction of load. Generally the experimental setup was in accordance with that reported by Sharma *et al.*[34]

2.6 OPV Fabrication and Testing

NP OPV devices were fabricated of architecture ITO/PEDOT:PSS/P3HT:PC_{61}BM NP/Ca/Al (Figure 5a) and ITO/PEDOT:PSS/P3HT:PC_{61}BM NP/ZnO/Al. Indium tin oxide (ITO)

substrates were UV-ozone treated for 20 minutes. PEDOT:PSS (HTL Solar) was spin coated onto ITO at 5000 RPM (1 min). PEDOT:PSS films were dried on a hotplate at 140 °C, 20 min. Nanoparticle films were spin coated (35 μl) at 1750 RPM (or 1500 and 1250 RPM for Table S1 and Figure S3). Nanoparticle films were dried on a hotplate for 4 min. at 110 °C. Ca (30 nm) and Al (110 nm) were deposited under vacuum conditions (10^{-6} Torr) via thermal evaporation using an Angstrom Amod deposition system. For the varied active layer film thickness study, the film thickness was measured on a Bruker DektakXT profilometer and the values are listed in Table 1. Note that thermal annealing treatments resulted in a shrinkage of film (decrease in film thickness, Table 1) as the nanoparticles sinter together and void spaces are filled, consistent with reports by Xie *et al.*[15]

Table 1. Rapid evaporation P3HT:$PC_{61}BM$ nanoparticle (RE-NP) film thickness with varied spin coater speed. Measurements taken following spin coating, as well as following drying (110 °C 4 min) and annealing (80 °C 4 min) treatments. Average film thickness is listed with standard deviation in parentheses.

Spin speed (RPM)	Film thickness as cast (nm) (σ)	Film thickness post-drying and annealing (nm) (σ)
1750	97 (8)	76 (21)
1500	115 (16)	98 (18)
1250	137 (14)	110 (24)

Current density-voltage (J-V) measurements were conducted using a Newport Class A solar simulator with an AM1.5 spectrum filter. The light intensity was measured to be 100 mW/cm² by a silicon reference solar cell (FHG-ISE) and the J-V data were recorded with a Keithley 2400 source meter. The OPV devices were masked during testing under AM 1.5 conditions, the masked area was 4 mm², all reported data is from masked devices. OPV devices were annealed at 80, 100 or 120 °C for 4 min. and re-tested.

3. Results and Discussion

Nanoparticles of the polymer donor material P3HT and the fullerene acceptor material $PC_{61}BM$ were fabricated via the miniemulsion method[18] with one key variation to the process reported in our previous studies[25,27,28,35] applied - namely a vacuum-assisted oil phase solvent removal step to accelerate the solvent removal. Nanoparticles prepared via this modified fabrication method will herein be referred to as rapid evaporation nanoparticles (RE-NPs). The size of the RE-NPs was measured by applying a circular Hough transform algorithm to SEM images of spin coated nanoparticle films consistent with our previously reported method;[28] SEM of the

RE-NPs is presented in Figure 2c. This analysis gave a mean particle diameter of 32 ± 12 nm for the RE-NPs. The same analysis was performed for nanoparticles prepared via the standard slow chloroform evaporation method (where chloroform is removed overnight on a hotplate set to 60 °C and 1200 RPM), which gave a mean diameter of 29 ± 12 nm (Figure 2d). Nanoparticles prepared via the standard slow chloroform evaporation method will herein be referred to as slow evaporation nanoparticles (SE-NPs). Considering the minimal difference in nanoparticle size with the modified fabrication method the changes observed in particle morphology, thermomechanical characteristics and fluorescence which will now be discussed cannot be attributed to nanoparticle size.

PL and UV-Visible absorbance measurements were performed on nanoparticle films (Figure 2a and b) and nanoparticle dispersions in water (Figure S1) prepared via both rapid and slow evaporation methods. PL is a valuable tool for probing variations in photoinduced processes within different active layer morphologies. Excitons that do not reach and dissociate at a donor-acceptor material interface in their lifetime will decay back to the ground state and lose the absorbed energy through radiative and non-radiative decay. PL can be used to probe the exciton population that undergoes radiative decay and to gauge donor material domain size and donor-acceptor phase intermixing. Assuming that the non-radiative decay and inter-system crossing rates do not change, the η_{ED} can be accurately determined using steady-state PL measurements. The PL spectra of both RE-NP and SE-NP films display P3HT 0-0 and vibronic 0-1 transitions at 650 and 690 nm,[36] respectively, and the UV-Vis absorbance spectra exhibit vibronic peaks characteristic of crystalline P3HT.[37] This feature is in comparison to a P3HT:PC$_{61}$BM BHJ film spin cast from chloroform solution, with no subsequent thermal annealing, which exhibits only a 0-0 peak in the PL spectrum and no vibronic shoulder peaks in the UV-Vis spectrum (Figure S2), characteristic of a highly intermixed donor-acceptor film morphology with no crystalline polymer domains. When comparing the RE-NP film PL to the SE-NP film PL, a reduction in signal intensity is observed with rapid evaporation. This reduction can be attributed to a higher degree of exciton quenching due to a higher degree of intermixing of donor and acceptor. The change in PL was quantified by calculating η_{ED} using equations 1 and 2 (Supplementary Material). The PL in this equation is proportional to the number of photons (PL as measured × wavelength). The constant background level was subtracted, the corrected PL signal was integrated between λ = 850 and 600 nm, and then divided by the absorption fraction of the film at the excitation wavelength of 500 nm (%A$_{500}$) (Equation 1). The PL of the P3HT:PC$_{61}$BM nanoparticles (PL_c^{Blend}) was then compared to the PL of pure P3HT

nanoparticles (PL_c^{P3HT}), subtracting this value from one gave the η_{ED} (Equation 2). An η_{ED} of 44% was calculated for the SE-NPs; this value increased to 50% for the RE-NPs.

To further quantify the difference in PL the change in P3HT 0-1 to 0-0 peak intensity was utilised. According to Spano *et al.*[38] the 0-1 to 0-0 intensity ratio is highly sensitive to structural disorder, hence we have herein associated the 650 nm/0-0 transition with amorphous P3HT and the 690 nm/0-1 transition with crystalline P3HT. We have utilised the E_{0-1}/E_{0-0} peak ratio as a figure of merit to compare the fraction of crystalline P3HT to amorphous P3HT in blend films in this study, where a higher E_{0-1}/E_{0-0} ratio indicates a larger fraction of crystalline P3HT. For the nanoparticle film PL presented in Figure 2a, the E_{0-1}/E_{0-0} ratio is 0.97 for RE-NPs and 1.08 for SE-NPs, indicating that the RE-NPs contain a lower fraction of crystalline P3HT. The spherical shape of the RE-NPs when comparing electron micrographs of various nanoparticle types also indicates a lower fraction of crystalline P3HT (Figure S4), as nanoparticles containing crystalline domains of P3HT have been shown to possess a wrinkled and angular surface texture and shape.[39] We hypothesise that both the lower fraction of crystalline P3HT and the higher degree of donor-acceptor material intermixing in the RE-NPs is due to the reduced time period available for the materials to self-organise and form ordered nano-domains in the nanoparticle formation process.
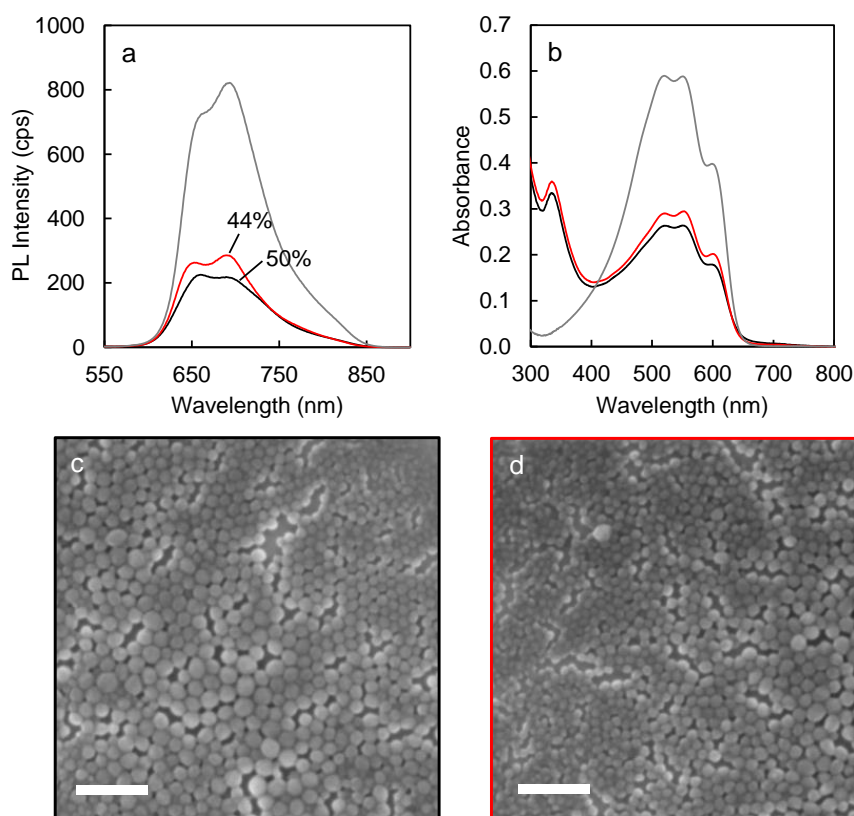

9

Figure 2. (a) Photoluminescence (PL) and (b) UV-Vis absorbance spectra of RE-NP film (solid black line), SE-NP film (solid red line) and pure P3HT nanoparticle film (solid grey line). Calculated η_{ED} of RE-NP and SE-NP films presented in (a). Scanning electron microscopy (SEM) images of (c) RE-NP monolayers and (d) SE-NP monolayers. Scale bars are 200 nm.

The internal morphology of the RE-NPs was further probed by STXM, a technique which utilises the chemical sensitivity of near edge X-ray absorption fine structure (NEXAFS) spectroscopy to resolve structure at the nanoscale. STXM maps of large RE-NPs revealed a core-shell morphology (Figure 3), and STXM maps of SE-NPs are presented in Figure S5 for comparison. The core-shell morphology of the RE-NPs is consistent with our previous reports of P3HT:$PC_{61}BM$ nanoparticles prepared with the slow evaporation method (and a similar P3HT molecular weight, M_n of 13,300 g mol^{-1}, PDI 1.2) albeit with varied domain compositions.[24] For the RE-NPs we observe a P3HT-rich shell composition of 64 ± 4 % P3HT and a $PC_{61}BM$-rich core composition of 60 ± 10 % $PC_{61}BM$ (Table 2), which compares to a composition of 70 ± 3% P3HT and 79 ± 12% $PC_{61}BM$ for the respective phases for the SE-NPs (Table 2).[24] These domain compositions were calculated by first generating a mean radial composition profile and then subtracting the nanoparticle shell contribution to the measured nanoparticle centre composition to determine the nanoparticle core composition (with further detail of the method reported elsewhere).[24] These STXM results further support the hypothesis that the RE-NPs contain more intermixed donor-acceptor phases than the SE-NPs. With the nanoparticle core showing the largest change in composition when comparing the RE-NP system to the SE-NP system.

Table 2. Compositional analysis of P3HT:$PC_{61}BM$ RE-NP and SE-NP, as calculated from STXM maps.

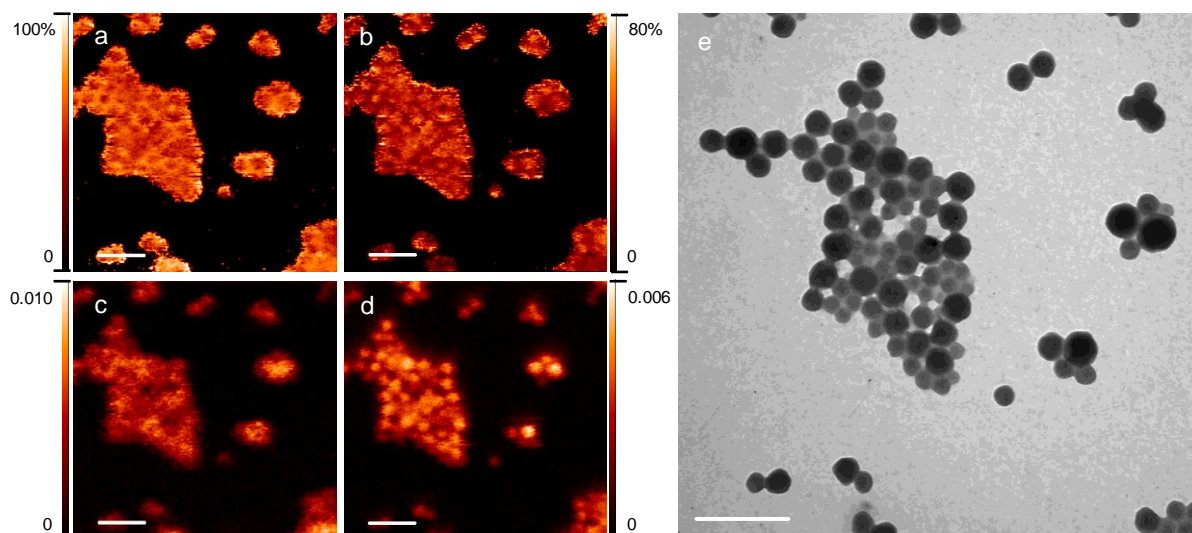| NP Type	Thermal Treatment Condition	P3HT composition of NP shell (%) (σ)	$PC_{61}BM$ composition of NP core (%) (σ)
SE-NP[24]	-	70 (3)	79 (12)
RE-NP	-	64 (4)	60 (10)
RE-NP	110 °C (4 min), 80 °C (4 min)	60 (9)	61 (15)

Figure 3. STXM fractional composition maps showing the concentration of (a) P3HT and (b) PC$_{61}$BM with corresponding STXM mass plots (c and d) and (e) position-matched TEM for unannealed 1:1 P3HT:PC$_{61}$BM RE-NPs. All scale bars are 500 nm. The colour contrast is scaled such that light colours correspond to higher component concentrations. For the mass plots (c and d) the colour scale bars indicate concentration of component in mg/cm^2.

Dynamic mechanical thermal analysis (DMTA), a technique usually applied to polymer films,[34] was applied to P3HT:PC$_{61}$BM nanoparticles. DMTA was utilised to determine the T$_g$ of the nanoparticles and their internal donor-acceptor phases. The 32 nm RE-NPs and 29 nm nm SE-NPs were cast onto a woven glass fibre mesh to obtain reinforced films and a sinusoidal stress was then applied to the sample, with a frequency of 1 Hz and amplitude of 5 μm, while the sample was exposed to a temperature increase at a rate of 3 °C/min to a maximum temperature of 300 °C. With DMTA, as the sample passes a phase change the elastic properties of the material change and this change can be measured by monitoring phase lag. Figure 4 presents the DMTA scans of RE-NPs and SE-NPs. Taking either the peak temperature in tan δ or the peak temperature in E'' (loss modulus) is the conventional approach of defining T$_g$ from DMTA measurements,[34,40,41] where tan δ = E''/E' and E' is the storage modulus. An order of magnitude drop in storage modulus can also signal a major material change. Consistent with Sharma *et al.*[34] we have utilised the tan δ peak to define the T$_g$ of the nanoparticle samples.

For both nanoparticle types, the features in the E' plots below 80 °C indicate that the nanoparticles are coalescing, potentially due to a softening of the polymer-rich nanoparticle shells at the T$_g$. For the RE-NP sample we observe a broad tan δ peak at 104 °C and for their slow evaporation counterpart (SE-NPs) a broad tan δ peak at 132 °C. Since neither the RE-NP system nor the SE-NP system contain pure material phases, these measured T$_g$s are likely to be

blend T_gs. Blend T_gs represent those of a blended binary phase, and will exist at a temperature between the T_g of the two pure components.[42] Sharma *et al.*[34] measured the T_g of pure P3HT to be 38 °C using this modified DMTA method. $PC_{61}BM$, being a non-polymer macromolecule, was more difficult to measure with the DMTA method,[34] hence we refer to our previous measurement of $PC_{61}BM$ NPs for the T_g determination of $PC_{61}BM$ giving a value of 161 °C.[39] The T_g of 132 °C measured for the SE-NPs is close to the T_g of pure $PC_{61}BM$, we hypothesise that this T_g is dominated by the nanoparticle core phase, which is the majority volume fraction of the SE-NPs. That is, the T_g of 132 °C represents the phase transition of the $PC_{61}BM$-rich (79 ± 12%) nanoparticle cores (P3HT:$PC_{61}BM$ blended phase, $T_g^{\text{blend SE}-\text{NP core}}$). By comparison, the T_g of 104 °C measured for the RE-NPs, near the midpoint of the two pure material T_gs, is indicative of a blended system. We hypothesise that the T_g of 104 °C is also dominated by the nanoparticle core phase and represents the phase transition of the $PC_{61}BM$-rich (60 ± 10 %) RE-NP cores (P3HT:$PC_{61}BM$ blended phase, $T_g^{\text{blend RE}-\text{NP core}}$) from a glassy to rubbery state. Hence the DMTA data supports the spectroscopy and microscopy data in revealing a more intermixed donor-acceptor morphology for the RE-NPs.
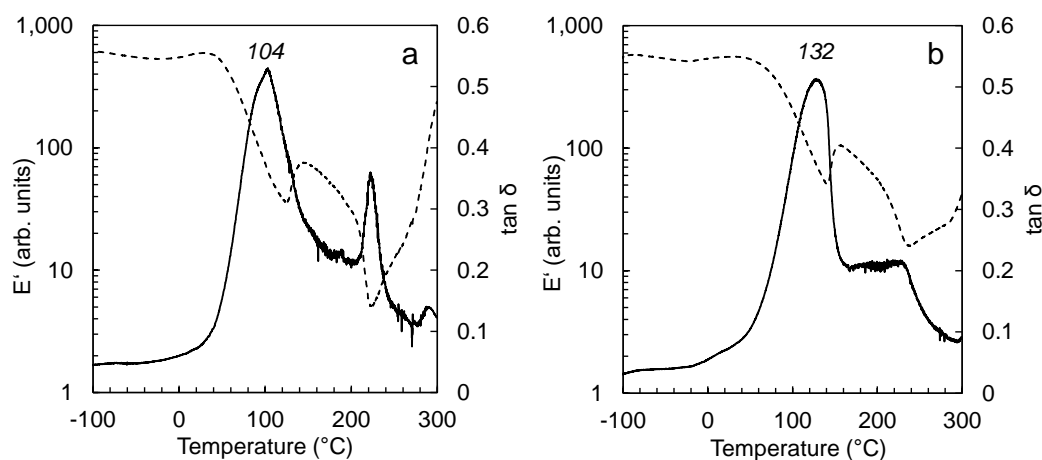

Figure 4. Dynamic mechanical thermal analysis (DMTA) temperature scans of (a) RE-NPs and (b) SE-NPs drop cast onto woven glass fibre mesh. Storage modulus (E') (dotted line) and tan δ (solid line) are presented.

NP OPV devices were fabricated from the 32 nm diameter RE-NPs in the conventional architecture to assess the effect of the varied fabrication method and internal nanoparticle morphology on device performance. Table 3 and Figure 5 show the RE-NP OPV device performance characteristics for devices with no post-cathode deposition thermal treatment (pre-CD TT) and for devices exposed to a post-cathode deposition thermal treatment (post-CD TT) of 80, 100 and 120 °C. The highest RE-NP OPV performance for unannealed (pre-CD TT)

devices was 1.0%, which is higher than the performance of unannealed SE-NP OPV devices reported previously (PCE 0.5 - 0.8% for 1:1 P3HT:PC$_{61}$BM SE-NP OPV).[25,27] This unannealed RE-NP OPV performance was further increased to 1.2% by utilising a ZnO electron transport layer (ETL) as an alternative to Ca (Table 3). SEM of a FIB-milled cross-section of an ITO/PEDOT:PSS/P3HT:PC$_{61}$BM RE-NP/ZnO/Al OPV device is provided in Figure 6, the SEM cross-section enabled the morphology of the photoactive layer to be imaged, which is quite uniform at a magnification of 100,000 x. Measurement of the RE-NP film thickness from the SEM cross-section gave a value of 71 nm, in good agreement with profilometry data listed in Table 1. The unannealed OPV device performance most closely represents the effect of the starting active layer morphology, hence an improvement in performance is indicative of a more optimal nanoparticle morphology and hence starting morphology of the photoactive layer in the RE-NP OPV devices. The highest PCE of annealed RE-NP OPV devices was also 1%, achieved with a post-CD TT of 80 °C, with the best device exhibiting an open circuit voltage (V$_{OC}$) of 405 mV, short circuit current density (J$_{SC}$) of 4.5 mA/cm^2 and a fill factor (FF) of 0.54. A post-CD TT of 80 °C is a temperature lower than that applied to similar P3HT:PC$_{61}$BM NP OPV devices in previous studies,[25] this lower temperature required to optimise OPV device performance indicates that a more intermixed donor-acceptor particle morphology requires a milder thermal treatment to sinter (or join) the particles and optimise bulk donor-acceptor film morphology. AFM measurements were recorded for RE-NP films on glass/ITO/PEDOT:PSS substrates (Figure S6) and demonstrate a good film coverage and clear nanoparticulate structure to the film. Temperatures higher than 80 °C resulted in a drop in V$_{OC}$ to 272 mV, J$_{SC}$ to 3.7 mA/cm^2 and FF to 0.33 leading to the reduction in PCE to 0.3% at 120 °C, although no observable gross phase separation is apparent in SEM (Figure S7b).

Table 3. RE-NP OPV device characteristics of best devices for varied post-cathode deposition thermal treatment (Post-CD TT) temperatures (TT time = 4 min), all devices were exposed to a pre-cathode deposition thermal treatment (Pre-CD TT) at 110 °C 4 min. The averages ± standard deviation are in parentheses.

Post-CD TT Temperature (°C)	ETL	V$_{OC}$ (mV)	J$_{SC}$ (mA/cm^2)	FF	PCE (%)
None	Ca	450 (439 ± 7)	4.0 (4.1 ± 0.2)	0.55 (0.50 ± 0.03)	1.0 (0.9 ± 0.1)
None	ZnO	380 (360 ± 10)	7.1 (5.9 ± 0.5)	0.44 (0.41 ± 0.02)	1.2 (0.9 ± 0.1)
80	Ca	405 (419 ± 19)	4.5 (4.0 ± 0.5)	0.54 (0.52 ± 0.02)	1.0 (0.8 ± 0.1)

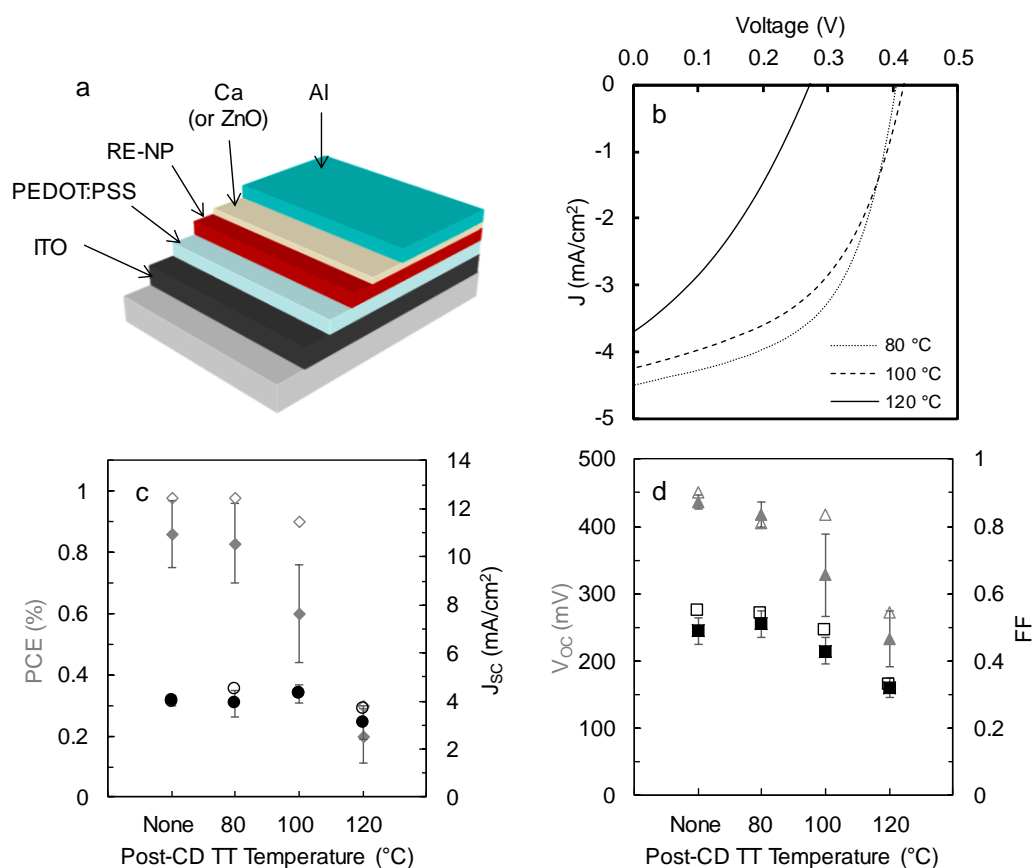|					
100	Ca	417 (328 ± 61)	4.3 (4.3 ± 0.4)	0.49 (0.43 ± 0.04)	0.9 (0.6 ± 0.2)
120	Ca	272 (233 ± 41)	3.7 (3.1 ± 0.7)	0.33 (0.32 ± 0.03)	0.3 (0.2 ± 0.1)

Figure 5. (a) OPV device architecture, (b) current density – voltage curves for best performing RE-NP OPVs (with Ca ETL) exposed to a post-cathode deposition thermal treatment (Post-CD TT) temperature of 80 °C (dotted line), 100 °C (dashed line) or 120 °C (solid line) (All devices were exposed to a pre-cathode deposition thermal treatment (Pre-CD TT) at 110 °C 4 min). (c) Average device power conversion efficiency (PCE) (grey closed diamond), best device PCE (grey open diamond), average device J_{SC} (black closed circle), best device J_{SC} (grey open circle), and (d) average device V_{OC} (grey closed triangle), best device V_{OC} (grey open triangle), average device fill factor (black closed square), best device fill factor (black open square) for varied post-CD TT temperature. Error bars represent the standard deviation in 6-24 replicate devices.
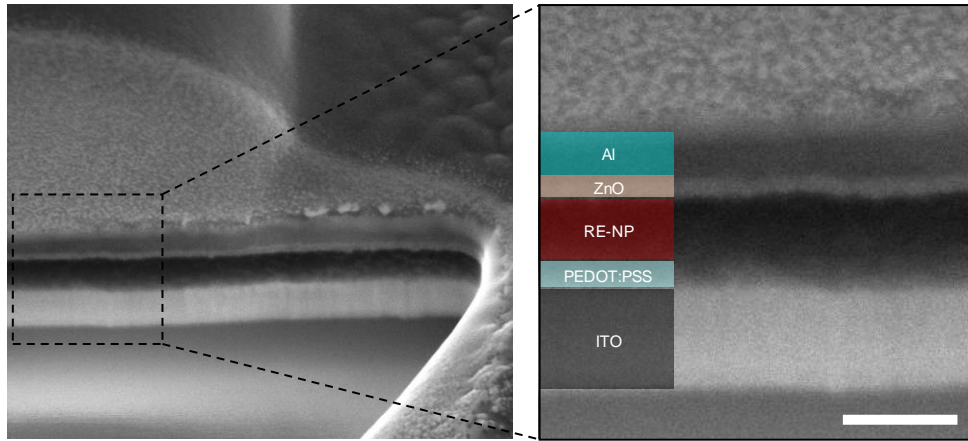
Figure 6. SEM of FIB-milled cross-section of an ITO/PEDOT:PSS/P3HT:PC$_{61}$BM RE-NP/ZnO/Al OPV device following annealing at 80 °C. Note that upon the Al layer, there is an Au and Pt layer visible in the micrograph, added to facilitate FIB-SEM measurement. The glass substrate is also visible in the micrograph. Scale bar is 100 nm.

PL and UV-Visible absorbance measurements were performed on RE-NP films exposed to thermal treatments matching OPV device fabrication thermal treatments (Figure 7a – b). The changes in PL and η_{ED} can be attributed to two processes in the nanoparticulate films.[39] Softening of the nanoparticles (*Process 1*) leads to an increase in contact surface area between nanoparticles and sintering of P3HT-rich nanoparticle shells effectively forming larger P3HT domains (an interconnected P3HT-rich shell network). In contrast, diffusion of PC$_{61}$BM from the PC$_{61}$BM nanoparticles into the amorphous P3HT fraction (*Process 2*) can alter the donor-acceptor ratio of blended domains. The thermal treatment of 110 °C 4 min resulted in an increase in observed PL from the samples, which caused a corresponding decrease of η_{ED} from 50% for the untreated film to 29% for the thermally treated film. An increase in PL of donor-acceptor material blend films following thermal treatment is usually attributed to phase separation,[43] a film morphological change constituting an increase in size and/or purity of the donor and acceptor material phases, or one of the two phases. Here we attribute the reduction of η_{ED} to be a result of the increase in size of the P3HT polymer phase as the polymer-rich nanoparticle shells sinter together as observed with SEM (Figure 2c and Figure 7c). This sintering of polymer-rich nanoparticle shells with thermal treatment has been reported previously.[27,28] A second thermal treatment at 80 °C 4 min (applied after the 110 °C 4 min treatment) then led to an increase in η_{ED} from 29 to 44%. We attribute this increase to a small degree of intermixing of the polymer and fullerene phases, which is possible at temperatures close to the blend T$_g$ of systems which contain molecularly mixed donor-acceptor phases rather than simply pure phases.[42,44] The change in composition of the RE-NP shells from 64 ± 4% to

60 ± 9% (Figure 8 and Table 2) following annealing accounts for this increase in η_{ED}. We propose that this intermixing process also occurred during the 110 °C treatment, although according to our previous report[27] a temperature of 110 °C causes minimal change to P3HT-rich nanoparticle shell composition, and hence the small degree of intermixing (*Process 2*) at 110 °C is overshadowed by the dominant morphological change of P3HT-rich nanoparticle shell sintering (*Process 1*). The observed increase in PL (reduction in η_{ED}) (Figure 7) confirms that the morphological change comprising the sintering of the P3HT-rich nanoparticle shells is the dominant process during the 110 °C post-film deposition treatment.
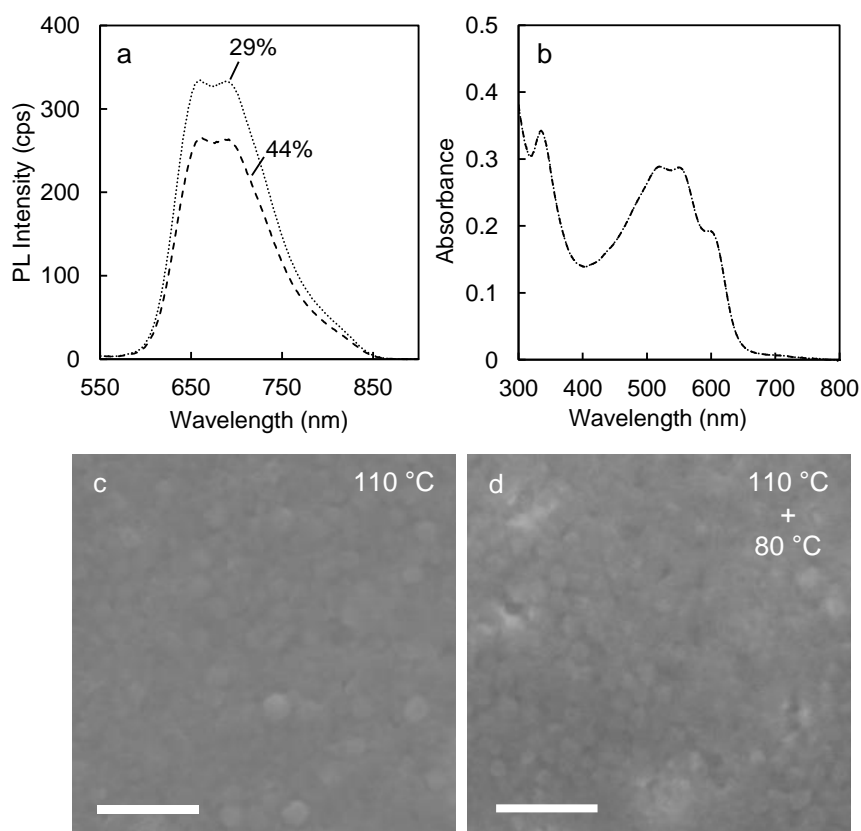

Figure 7. (a) Photoluminescence (PL) and (b) UV-Vis spectra of RE-NP film following 110 °C 4 min thermal treatment (dotted line) and following an additional 80 °C 4 min. thermal treatment (dashed line) to match OPV fabrication conditions. Calculated η_{ED} of RE-NP films exposed to each thermal treatment presented in (a). SEM images of RE-NP film thermally treated at (c) 110 °C for 4 min, (d) 110 °C 4 min followed by 80 °C 4 min. Scale bars are 200 nm.

A key requirement of an OPV photoactive layer is bicontinuous donor and acceptor material networks with nanoscale phase separation for efficient charge separation and transport.[6] Yu *et al.*[45] made a significant contribution to the research field with the introduction of the bulk heterojunction (BHJ) in 1995, leading to an improvement in η_{ED} over bilayer devices.[46] In this

current paper we have aimed to achieve an OPV active layer morphology as similar to a BHJ as possible but utilising a water-based photoactive ink deposition in order to take advantage of the eco-friendly nature of this deposition process. Previous studies of P3HT:PC$_{61}$BM NP OPV have reported a polymer-rich nanoparticle shell and fullerene-rich nanoparticle core.[24,47] Such a morphology is not ideal for photogeneration of charge and has led to a low exciton dissociation efficiency ($\eta_{ED} = 24\%$) and low internal quantum efficiency as reported by Al-Mudhaffer *et al.*[23] Other reports have claimed that one of the major areas that requires improvement in NP OPV is the exciton dissociation efficiency.[48,49] Here we have been successful in generating a more blended nanoparticle morphology, something closer to a traditional BHJ morphology, by using a rapid miniemulsion dispersed phase solvent removal step to "lock-in" a blended donor-acceptor morphology before the two materials have sufficient time to move to their respective domains (core and shell) driven by the difference in their surface energies.[47] This internal nanoparticle morphology is essentially locked in at a stage before thermodynamic equilibrium has been reached. This improved morphology resulted in an increased η_{ED} over previous studies, with a value of 50% achieved. Regardless of the improvement in η_{ED} the PCE of the RE-NP OPV devices is yet to match BHJ OPVs; this result indicates that contrary to the work of Al-Mudhaffer *et al.*[23] the dominate loss mechanism in P3HT:PC$_{61}$BM NP OPV of inefficient charge generation cannot be resolved by improving the donor-acceptor mixing in the nanoparticulate structure (or simply photoactive layer morphology). The RE-NP study suggests that there are other factors at play which still require further research effort in order for eco-friendly nanoparticle inks to be brought to a competitive level. Xie *et al.*[22] summarise the residual performance gap between halogenated solvent processing and aqueous nanoparticle processing to be attributed to three loss mechanisms: (a) residual surfactant (stabiliser) in the photoactive layer, (b) inconsistent film quality caused by poor wetting of aqueous nanoparticle inks, and (c) improper distribution of the donor and acceptor material domains in the nanoparticle system. Our study indicates that the third mechanism identified by Xie *et al.*[22] is not the major contributor to loss of performance in NP OPV. The presence of excess surfactant within the photoactive layer is suggested to be the major hindrance of performance, as demonstrated very recently by Xie *et al.*,[50] who achieved significant improvements in NP OPV performance upon the removal of 98% of residual surfactant from nanoparticle dispersions prior to film deposition, as a result of improved charge transport through the photoactive layer. Moving forward, the development of a methodology incorporating both the improved intermixing of donor and acceptor phases, and the removal of

excess surfactant within the photoactive layer has the potential to advance the performance of NP OPV to a competitive level.
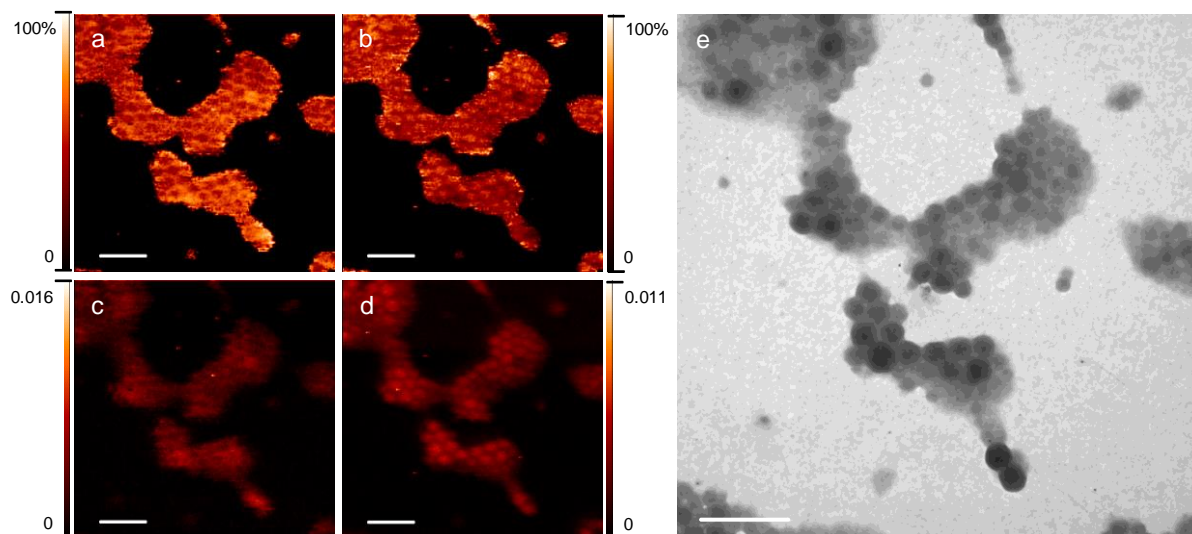

Figure 8. STXM fractional composition maps showing the concentration of (a) P3HT and (b) PC$_{61}$BM with corresponding STXM mass plots (c and d) and (e) position-matched TEM for 1:1 P3HT:PC$_{61}$BM RE-NPs dried at 110 °C for 4 min followed by annealing at 80 °C for 4 min. All scale bars are 500 nm. The colour contrast is scaled such that light colours correspond to higher component concentrations. For the mass plots (c and d) the colour scale bars indicate concentration of component in mg/cm^2.

4. Conclusions

A modified miniemulsion nanoparticle fabrication procedure was developed involving the use of a vacuum-assisted miniemulsion dispersed phase solvent removal step, resulting in a five-fold decrease in the nanoparticle fabrication time as well as improving the intermixing of donor and acceptor materials within the nanoparticles. This improved nanoparticle morphology was characterised using a combination of STXM, UV-vis spectroscopy and PL spectroscopy measurements. Additionally, DMTA of the nanoparticle inks revealed a T$_g$ of 104 °C rather than a T$_g$ characteristic of a pure polymer or pure fullerene phases, further demonstrating a highly intermixed internal nanoparticle morphology. This methodology achieved an increased η_{ED} of 50% compared with the standard miniemulsion nanoparticle fabrication procedure, and PCEs of up to 1.2% were achieved using the P3HT:PC$_{61}$BM material system, similar to previous reports for core-shell nanoparticles. As such, we show here that creating a more intermixed donor-acceptor nanoparticle morphology is not the standalone solution to enhancing NP OPV device performance.

Conflicts of Interest

There are no conflicts of interest to declare.

Acknowledgements

Supplementary Material

Supplementary data associated with this article can be found in the online version.

References

1   K. A. Mazzio and C. K. Luscombe, The future of organic photovoltaics, *Chem. Soc. Rev.*, 2015, **44**, 78–90.

2   F. C. Krebs, N. Espinosa, M. Hösel, R. R. Søndergaard and M. Jørgensen, 25th Anniversary article: Rise to power – OPV-based solar parks, *Adv. Mater.*, 2014, **26**, 29–39.

3   F. Machui, M. Hösel, N. Li, G. D. Spyropoulos, T. Ameri, R. R. Søndergaard, M. Jørgensen, A. Scheel, D. Gaiser, K. Kreul, D. Lenssen, M. Legros, N. Lemaitre, M. Vilkman, M. Välimäki, S. Nordman, C. J. Brabec and F. C. Krebs, Cost analysis of roll-to-roll fabricated ITO free single and tandem organic solar modules based on data from manufacture, *Energy Environ. Sci.*, 2014, **7**, 2792–2802.

4   Z. Ding, V. Stoichkov, M. Horie, E. Brousseau and J. Kettle, Spray coated silver nanowires as transparent electrodes in OPVs for building integrated photovoltaics applications, *Sol. Energy Mater. Sol. Cells*, 2016, **157**, 305–311.

5   X. Gu, Y. Zhou, K. Gu, T. Kurosawa, Y. Guo, Y. Li, H. Lin, B. C. Schroeder, H. Yan, F. Molina-Lopez, C. J. Tassone, C. Wang, S. C. B. Mannsfeld, H. Yan, D. Zhao, M. F. Toney and Z. Bao, Roll-to-roll printed large-area all-polymer solar cells with 5% efficiency based on a low crystallinity conjugated polymer blend, *Adv. Energy Mater.*, 2017, **7**, 1602742.

6   Z. Xiao, X. Jia and L. Ding, Ternary organic solar cells offer 14% power conversion efficiency, *Sci. Bull.*, 2017, **62**, 1562–1564.

7   C. H. Peters, I. T. Sachs-Quintana, J. P. Kastrop, S. Beaupré, M. Leclerc and M. D. McGehee, High efficiency polymer solar cells with long operating lifetimes, *Adv. Energy Mater.*, 2011, **1**, 491–494.

8   S. Zhang, L. Ye, H. Zhang and J. Hou, Green-solvent-processable organic solar cells, *Mater. Today*, 2016, **19**, 533–543.

9   M. Bag, T. S. Gehan, D. D. Algaier, F. Liu, G. Nagarjuna, P. M. Lahti, T. P. Russell and D. Venkataraman, Efficient charge transport in assemblies of surfactant-stabilized semiconducting nanoparticles, *Adv. Mater.*, 2013, **25**, 6411–6415.

10   M. M. Voigt, F. Machui, L. Lucera, G. Spyropoulos, J. Cordero, P. Kubis, A. S. Ali, A. E. Shalan and C. J. Brabec, Tailoring green formulation: Printing and upscaling of inverted organic solar cells, *Conf. Rec. IEEE Photovolt. Spec. Conf.*, 2013, 3092–3097.

11   S. Sankaran, K. Glaser, S. Gärtner, T. Rödlmeier, K. Sudau, G. Hernandez-Sosa and A. Colsmann, Fabrication of polymer solar cells from organic nanoparticle dispersions by doctor blading or ink-jet printing, *Org. Electron.*, 2016, **28**, 118–122.

12   T. R. Andersen, T. T. Larsen-Olsen, B. Andreasen, A. P. L. Böttiger, J. E. Carlé, M. Helgesen, E. Bundgaard, K. Norrman, J. W. Andreasen, M. Jørgensen and F. C. Krebs, Aqueous processing of low-band-gap polymer solar cells using roll-to-roll methods., *ACS Nano*, 2011, **5**, 4188–4196.

13   S. Gärtner, M. Christmann, S. Sankaran, H. Röhm, E.-M. Prinz, F. Penth, A. Pütz, A. E. Türeli, B. Penth, B. Baumstümmler and A. Colsmann, Eco-friendly fabrication of 4% efficient organic solar cells from surfactant-free P3HT:ICBA nanoparticle dispersions, *Adv. Mater.*, 2014, **26**, 6653–6657.

14   F. J. M. Colberts, M. M. Wienk and R. A. J. Janssen, Aqueous nanoparticle polymer

solar cells: Effects of surfactant concentration and processing on device performance, *ACS Appl. Mater. Interfaces*, 2017, **9**, 13380−13389.

15   C. Xie, A. Classen, A. Späth, X. Tang, J. Min, M. Meyer, C. Zhang, N. Li, A. Osvet, R. H. Fink and C. J. Brabec, Overcoming microstructural limitations in water processed organic solar cells by engineering customized nanoparticulate inks, *Adv. Energy Mater.*, 2018, **8**, 1702857.

16   N. A. D. Yamamoto, M. E. Payne, M. Koehler, A. Facchetti, L. S. Roman and A. C. Arias, Charge transport model for photovoltaic devices based on printed polymer:fullerene nanoparticles, *Sol. Energy Mater. Sol. Cells*, 2015, **141**, 171–177.

17   T. S. Gehan, M. Bag, L. A. Renna, X. Shen, D. D. Algaier, P. M. Lahti, T. P. Russell and D. Venkataraman, Multiscale active layer morphologies for organic photovoltaics through self-assembly of nanospheres, *Nano Lett.*, 2014, **14**, 5238–5243.

18   K. Landfester, R. Montenegro, U. Scherf, R. Güntner, U. Asawapirom, S. Patil, D. Neher and T. Kietzke, Semiconducting polymer nanospheres in aqueous dispersion prepared by a miniemulsion process, *Adv. Mater.*, 2002, **14**, 651–655.

19   H. Shimizu, M. Yamada, R. Wada and M. Okabe, Preparation and characterization of water self-dispersible poly(3-hexylthiophene) particles, *Polym. J.*, 2008, **40**, 33–36.

20   D. Darwis, N. Holmes, D. Elkington, A. L. David Kilcoyne, G. Bryant, X. Zhou, P. Dastoor and W. Belcher, Surfactant-free nanoparticulate organic photovoltaics, *Sol. Energy Mater. Sol. Cells*, 2014, **121**, 99–107.

21   L. D'Olieslaeger, G. Pirotte, I. Cardinaletti, J. D'Haen, J. Manca, D. Vanderzande, W. Maes and A. Ethirajan, Eco-friendly fabrication of PBDTTPD:PC71BM solar cells reaching a PCE of 3.8% using water-based nanoparticle dispersions, *Org. Electron.*, 2017, **42**, 42–46.

22   C. Xie, X. Tang, M. Berlinghof, S. Langner, S. Chen, A. Späth, N. Li, R. H. Fink, T. Unruh and C. J. Brabec, Robot-based high-throughput engineering of alcoholic polymer: Fullerene nanoparticle inks for an eco-friendly processing of organic solar cells, *ACS Appl. Mater. Interfaces*, 2018, **10**, 23225–23234.

23   M. F. Al-Mudhaffer, M. J. Griffith, K. Feron, N. C. Nicolaidis, N. A. Cooling, X. Zhou, J. Holdsworth, W. J. Belcher and P. C. Dastoor, The origin of performance

limitations in miniemulsion nanoparticulate organic photovoltaic devices, *Sol. Energy Mater. Sol. Cells*, 2018, **175**, 77–88.

24 N. P. Holmes, K. B. Burke, P. Sista, M. Barr, H. D. Magurudeniya, M. C. Stefan, A. L. D. Kilcoyne, X. Zhou, P. C. Dastoor and W. J. Belcher, Nano-domain behaviour in P3HT:PCBM nanoparticles, relating material properties to morphological changes, *Sol. Energy Mater. Sol. Cells*, 2013, **117**, 437–445.

25 N. P. Holmes, S. Ulum, P. Sista, K. B. Burke, M. G. Wilson, M. C. Stefan, X. Zhou, P. C. Dastoor and W. J. Belcher, The effect of polymer molecular weight on P3HT:PCBM nanoparticulate organic photovoltaic device performance, *Sol. Energy Mater. Sol. Cells*, 2014, **128**, 369–377.

26 N. P. Holmes, B. Vaughan, E. L. Williams, R. Kroon, M. R. Anderrson, A. L. D. Kilcoyne, P. Sonar, X. Zhou, P. C. Dastoor and W. J. Belcher, Diketopyrrolopyrrole-based polymer:fullerene nanoparticle films with thermally stable morphology for organic photovoltaic applications, *MRS Commun.*, 2017, **7**, 67–73.

27 N. P. Holmes, N. Nicolaidis, K. Feron, M. Barr, K. B. Burke, M. Al-Mudhaffer, P. Sista, A. L. D. Kilcoyne, M. C. Stefan, X. Zhou, P. C. Dastoor and W. J. Belcher, Probing the origin of photocurrent in nanoparticulate organic photovoltaics, *Sol. Energy Mater. Sol. Cells*, 2015, **140**, 412–421.

28 N. P. Holmes, M. Marks, P. Kumar, R. Kroon, M. G. Barr, N. Nicolaidis, K. Feron, A. Pivrikas, A. Fahy, A. D. D. Z. Mendaza, A. L. D. Kilcoyne, C. Müller, X. Zhou, M. R. Andersson, P. C. Dastoor and W. J. Belcher, Nano-pathways: Bridging the divide between water-processable nanoparticulate and bulk heterojunction organic photovoltaics, *Nano Energy*, 2016, **19**, 495–510.

29 Y. Wang, H. Zhu, Z. Shi, F. Wang, B. Zhang, S. Dai and Z. Tan, Engineering the vertical concentration distribution within the polymer:fullerene blends for high performance inverted polymer solar cells, *J. Mater. Chem. A*, 2017, **5**, 2319–2327.

30 C. Li, H. Zhu, Y. Wang, H. Liu, S. Hu, F. Wang, B. Zhang, S. Dai and Z. Tan, High performance polymer solar cells with electron extraction and light-trapping dual functional cathode interfacial layer, *Nano Energy*, 2017, **31**, 201–209.

31 Z. Shi, H. Liu, Y. Wang, J. Li, Y. Bai, F. Wang, X. Bian, T. Hayat, A. Alsaedi and Z.

Tan, Incorporating an Electrode Modification Layer with a Vertical Phase Separated Photoactive Layer for Efficient and Stable Inverted Nonfullerene Polymer Solar Cells, *ACS Appl. Mater. Interfaces*, 2017, **9**, 43871–43879.

32   J. C. Hummelen, B. W. Knight, F. Lepeq, F. Wudl, J. Yao and C. L. Wilkins, Preparation and characterization of fulleroid and methanofullerene derivatives, *J. Org. Chem.*, 1995, **60**, 532–538.

33   A. L. D. Kilcoyne, T. Tyliszczak, W. F. Steele, S. Fakra, P. Hitchcock, K. Franck, E. Anderson, B. Harteneck, E. G. Rightor, G. E. Mitchell, A. P. Hitchcock, L. Yang, T. Warwick and H. Ade, Interferometer-controlled scanning transmission X-ray microscopes at the Advanced Light Source, *J. Synchrotron Radiat.*, 2003, **10**, 125–136.

34   A. Sharma, X. Pan, J. A. Campbell, M. R. Andersson and D. A. Lewis, Unravelling the thermomechanical properties of bulk heterojunction blends in polymer solar cells, *Macromolecules*, 2017, **50**, 3347–3354.

35   B. Vaughan, E. L. Williams, N. P. Holmes, P. Sonar, A. Dodabalapur, P. C. Dastoor and W. J. Belcher, Water-based nanoparticulate solar cells using a diketopyrrolopyrrole donor polymer, *Phys. Chem. Chem. Phys.*, 2014, **16**, 2647–2653.

36   D. E. Motaung, G. F. Malgas, C. J. Arendse, S. E. Mavundla and D. Knoesen, Structural and photo-physical properties of spin-coated poly(3-hexylthiophene) thin films, *Mater. Chem. Phys.*, 2009, **116**, 279–283.

37   T. A. Chen, X. Wu and R. D. Rieke, Regiocontrolled synthesis of poly(3-alkylthiophenes) mediated by Rieke zinc: Their characterization and solid-state properties, *J. Am. Chem. Soc.*, 1995, **117**, 233–244.

38   F. C. Spano, J. Clark, C. Silva and R. H. Friend, Determining exciton coherence from the photoluminescence spectral line shape in poly(3-hexylthiophene) thin films., *J. Chem. Phys.*, 2009, **130**, 74904.

39   N. P. Holmes, M. Marks, J. M. Cave, K. Feron, M. G. Barr, A. Fahy, A. Sharma, X. Pan, D. A. L. Kilcoyne, X. Zhou, D. A. Lewis, M. R. Andersson, J. van Stam, A. B. Walker, E. Moons, W. J. Belcher and P. C. Dastoor, Engineering two-phase and three-phase microstructures from water-based dispersions of nanoparticles for eco-friendly

polymer solar cell applications, *Chem. Mater.*, 2018, **30**, 6521−6531.

40   P. E. Hopkinson, P. A. Staniec, A. J. Pearson, A. D. F. Dunbar, T. Wang, A. J. Ryan, R. A. L. Jones, D. G. Lidzey and A. M. Donald, A phase diagram of the P3HT:PCBM organic photovoltaic system: Implications for device processing and performance, *Macromolecules*, 2011, **44**, 2908–2917.

41   B. K. Kuila and A. K. Nandi, Structural hierarchy in melt-processed poly(3-hexyl thiophene)-montmorillonite clay nanocomposites: Novel physical, mechanical, optical, and conductivity properties, *J. Phys. Chem. B*, 2006, **110**, 1621–1631.

42   C. Müller, On the glass transition of polymer semiconductors and its impact on polymer solar cell stability, *Chem. Mater.*, 2015, **27**, 2740–2754.

43   A. L. Ayzner, D. D. Wanger, C. J. Tassone, S. H. Tolbert and B. J. Schwartz, Room to improve conjugated polymer-based solar cells: Understanding how thermal annealing affects the fullerene component of a bulk heterojunction photovoltaic device, *J. Phys. Chem. C*, 2008, **112**, 18711–18716.

44   J. Bergqvist, C. Lindqvist, O. Bäcke, Z. Ma, Z. Tang, W. Tress, S. Gustafsson, E. Wang, E. Olsson, M. R. Andersson, O. Inganäs and C. Müller, Sub-glass transition annealing enhances polymer solar cell performance, *J. Mater. Chem. A*, 2014, **2**, 6146–6152.

45   G. Yu, J. Gao, J. C. Hummelon, F. Wudl and A. J. Heeger, Polymer photovoltaic cells: Enhanced efficiencies via a network of internal donor-acceptor heterojunctions, *Science (80-.).*, 1995, **270**, 1789–1791.

46   A. J. Heeger, 25th anniversary article: Bulk heterojunction solar cells: Understanding the mechanism of operation, *Adv. Mater.*, 2014, **26**, 10–28.

47   S. Ulum, N. Holmes, D. Darwis, K. Burke, A. L. David Kilcoyne, X. Zhou, W. Belcher and P. Dastoor, Determining the structural motif of P3HT:PCBM nanoparticulate organic photovoltaic devices, *Sol. Energy Mater. Sol. Cells*, 2013, **110**, 43–48.

48   M. Bag, T. S. Gehan, L. A. Renna, D. D. Algaier, P. M. Lahti and D. Venkataraman, Fabrication conditions for efficient organic photovoltaic cells from aqueous dispersions of nanoparticles, *RSC Adv.*, 2014, **4**, 45325–45331.

49   X. Han, M. Bag, T. S. Gehan, D. Venkataraman and D. Maroudas, Analysis of charge transport and device performance in organic photovoltaic devices with active layers of self-assembled nanospheres, *J. Phys. Chem. C*, 2015, **119**, 25826–25839.

50   C. Xie, T. Heumüller, W. Gruber, X. Tang, A. Classen, I. Schuldes, M. Bidwell, A. Späth, R. H. Fink, T. Unruh, I. Mcculloch, N. Li and C. J. Brabec, Overcoming efficiency and stability limits in water-processing nanoparticular organic photovoltaics by minimizing microstructure defects, *Nat. Commun.*, 2018, **9**, 5335.